The Effects of Wheel Design on the Aerodynamic Drag of Passenger Vehicles

2019-01-0662

The Effects of Wheel Design on the Aerodynamic Drag of Passenger Vehicles

Author, co-author (Do NOT enter this information. It will be pulled from participant tab in MyTechZone)

Affiliation (Do NOT enter this information. It will be pulled from participant tab in MyTechZone)

Abstract

Approximately 25 % of a passenger vehicle's aerodynamic drag comes directly or indirectly from its wheels, indicating that the rim geometry is highly relevant for increasing the vehicle's overall energy efficiency. An extensive experimental study is presented where a parametric model of the rim design was developed, and statistical methods were employed to isolate the aerodynamic effects of certain geometric rim parameters. In addition to wind tunnel force measurements, this study employed the flowfield measurement techniques of wake surveys, wheelhouse pressure measurements, and base pressure measurements to investigate and explain the most important parameters' effects on the flowfield. In addition, a numerical model of the vehicle with various rim geometries was developed and used to further elucidate the effects of certain geometric parameters on the flow field. The results showed that the most important parameter was the coverage area, and it was found to have a linear effect on the aerodynamic drag. Interestingly, parameters associated with the outer radial region of wheel (rim cover) were also found to be significant, along with the wheel depth of center (flatness). The flowfield measurements showed, again, that the coverage area had the most significant effect, with it directly affecting how much flow passes through the front rim and subsequently affecting features like the near-ground jetting vortex and vortices out of the wheelhouse. In addition, the coverage area also affected the pressure recovery at the base of the vehicle and the wheelhouse pressure. The effects of other parameters are also detailed in the paper. The effects of different coverage area at the front and rear rims on the drag coefficient were investigated, where having a high coverage at the rear reduced drag the most.

Introduction

Aerodynamics greatly affects a passenger vehicle's performance, with the drag comprising over 50% of the total resistive force above 70 km/h [1-3]. As a result of increasingly strict emissions regulations [4] and rising consumer demands, reducing the drag of passenger vehicles is becoming increasingly important.

The wheels of a vehicle account for approximately 25% of the overall drag coefficient of a passenger vehicle [5] and the rim's geometry significantly influences the drag [6-11]. When the flow reaches the front of the wheel, a stagnation point occurs and the flow divides. From this point, three main vortex structures occur; a jetting vortex, a shoulder vortex, and a top vortex [12-14]. Other vortices occur throughout the wheelhouse as well. Typically, the rim's coverage area affects the drag coefficient the most, with an inverse relationship typically found [6-10]. A previous study suggested that a fully covered wheel blocks the flow entering the front wheels, reduces the vortex size behind the tires and reduced flow separation at the wheels [15]. In addition, covering the rim from the rim track towards the center is more effective at reducing the drag coefficient than covering the rim from the center towards the rim track [8]. Furthermore, a larger wheel diameter typically increases the drag coefficient [6, 11]. While these trends have been found, the effects of the various rim features on the flowfield are typically uninvestigated, therefore, it is difficult to determine why these trends occur. In addition to these parameters, there are other parameters of interest, including the spoke shape, the rim depth of center, and the rim track design, which have not been investigated.

In addition to investigating the effects of rim features on all four rims on the drag coefficient, the effect of different front and rear rims has received attention, with the general conclusion being that the changes in the drag coefficient from the front and rear rims are independent of each other, and summate to give the overall change in the drag coefficient (no synergy) [8, 16]. Some flowfield measurements were detailed pertaining to the effects of different front and rear rim designs, however, it is difficult to determine from the reported figures if the flowfields displayed any synergy between the front and rear rims.

Methodology

The study utilized both experimental wind tunnel tests and numerical CFD simulations, to investigate the effects of various rim geometric parameters on the drag production and flowfield of passenger vehicles.

Experimental procedure

The experimental work was performed in the Volvo Aerodynamic Wind Tunnel at Volvo Car Corporation (VCC). The tunnel had a slotted wall test section, with a cross-sectional area of 27 m^2. The test section was further equipped with a 5-belt moving ground system, a boundary layer scoop and two distributed suction zones upstream of the 5-belt system, and tangential blowers behind the center belt and the wheels. Sufficient boundary layer control, and rotating wheels have been found vital for underbody and wheel analysis [17]. Four struts and the wheel drive units hold the vehicle in place and measure the aerodynamic forces acting on the vehicle. All tests were performed at 140 km/h at zero yaw angle. The wind tunnel

uncertainties at these conditions can be seen in Table 1. For a detailed description of the tunnel geometry and flow quality, the reader is referred to [18, 19].

Table 1. Measurement uncertainties, in terms of drag and lift coefficients, for a standard test case at 140 km/h in the Volvo Aerodynamic Wind Tunnel.

Test case	ΔC_D
Difference within the same test	0.001
Difference for the same vehicle, but difference test session	0.003

Test objects

The two test objects, a sedan type (Volvo S90) vehicle and an estate type (Volvo V90) vehicle, can be seen in Figure 1. Two sets of 18 inch wheels were used during the wind tunnel tests; a set of regular production wheels (PW), and the base wheels (BW) that were used in the modular wheel concept (further explained below). Both sets of wheels were equipped with new Michelin© Primacy 3 245/45 R18 tires of the same type, but from different manufacturing batches (i.e. the same tire geometry within manufacturing tolerances).

Figure 1. The test objects. Upper image is the sedan vehicle (Volvo S90), and below is the estate vehicle (Volvo V90). Coordinate system shown.

Modular wheel concept

A modular wheel concept was further developed, based on previous work [20], to enable cost and time efficient evaluation of many wheel geometries. This concept consisted of a thin BW, only to be used in the wind tunnel testing environment, on which 3D printed spoke geometries were mounted using a snap-fit design, see Figure 2. The rim geometry could thus be changed without removing the wheels or changing the vehicle position in the wind tunnel.

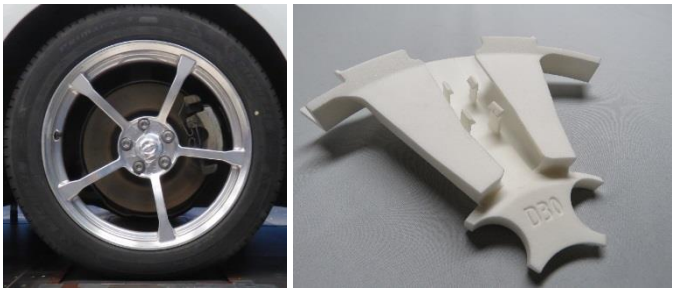

a) b)

Figure 2. The modular wheel concept consisting of a) the base wheel and b) the 3D printed plastic inserts.

Rim parameters

The study divided the rim into 14 independent generic parameters that could describe a large set of rim designs, see Table 2. Eleven (11) of these were put into the screening process, while the remaining parameters where known to have a significant effect on the aerodynamic drag prior to the study. The total coverage area (No. 1) was known to be important [21] and the number of spokes (No. 14) was a central styling parameter. Parameters 2-8 are shown in Figure 3a and parameters 9-13 are shown in Figure 3b.

Previous studies indicated that covering the rim (rim cover) near the rim track has a high influence on the aerodynamic drag production [21]. Hence, the three parameters No. 2, 3 and 4 were chosen to investigate this feature, where the rim cover distance (No. 2) is measured from the outer edge of the rim towards the center, see Figure 3a. Parameters No. 5 and 6 describe where the spoke bends towards the hub, and the depth of the hub, respectively. The drop angle (No. 7) is a design feature not affecting the coverage area but making the spoke top surface smaller by creating angled sides of the spoke. Lastly in Figure 3a, the spoke end radius (No. 8) is visualized.

Figure 3b displays parameter No. 9, a parameter determining if the spoke is concave or convex. It also shows the spoke edge radius (No. 10) and the spoke window width (No. 11), which are of interest from styling and aerodynamic perspectives. Finally, the rim track design (No. 13) is visualized.

Table 2. The numbered rim parameters and their evaluation occurrences in the first test session (screening) and the second test session (detailed parameter investigation).

No.	Name	Screening	DPI
1	Coverage area		X
2	Rim cover distance		X
3	Rim cover depth	X	X
4	Rim cover angle	X	X
5	Position of break	X	
6	Depth of center	X	X
7	Drop angle		X
8	Spoke end radius	X	
9	Concavity of spoke	X	
10	Spoke edge radius	X	
11	Spoke window width	X	X
12	Diamond cut	X	
13	Rim track design	X	
14	Number of spokes	X	

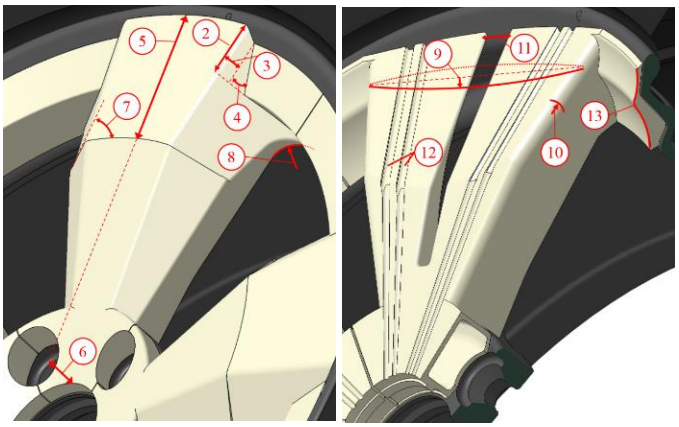

a) b)

Figure 3. Spoke showing parameters 2 to 8 (a) and spoke showing parameters 9 to 13 (b).

Evaluation procedure

The first part of the evaluation procedure was to verify that the modular wheel concept could yield the same results as regular production wheels. Hence, a representation of the PW using the modular wheel concept was compared to the real PW, see Figure 4. To estimate the influence from the different tire batches, additional tests with cover plates mounted onto both sets of the wheels were performed, see Figure 4. The tire batch influence could then be accounted for when evaluating the modular wheel concept.

Figure 4. Rim configurations used to evaluate the modular wheel concept: a covered wheel (left), a production wheel (middle) and a representation of production wheel (S19) using the modular wheel concept (right).

The coverage area was known to be important from a previous study [21] and was therefore also investigated separately at 40 %, 65 % and 90 % coverage, see Figure 5.

Figure 5. Rim configurations used to separately investigate the coverage area at 40 %, 65 % and 90 % coverage.

The force measurements study also included an investigation of different front and rear rim designs on the sedan, where the 40 % covered (D36) and 90 % covered (D38) rims where used. The first setup used 40 % coverage at the front and 90 % at the rear (F40R90). The inverse was used as the second setup (F90R40).

The purpose of the chosen evaluation procedure was to be able to formulate a mathematical regression model that could accurately predict drag changes when altering the rim parameters as inputs. To do so, a large number of parameters needed to be screened to enable a detailed investigation of only the most important parameters. This work flow is visualized in Figure 6, where the arrows indicate information transfer in terms of important parameters and experimental results. The screening was done during the first wind tunnel session, where only test object 1 was used. The detailed parameter investigation (DPI) was done during the second wind tunnel session, where both test objects were used.

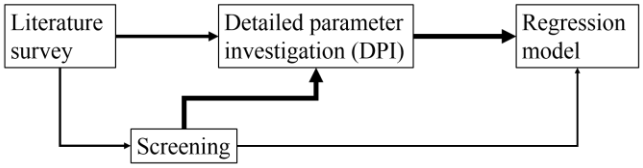

Figure 6. Flow chart of the statistical evaluation procedure.

Screening tests (1st test session)

The screening utilized a statistical Plackett-Burman design, where all synergies between parameters were assumed to be insignificant. This enabled a screening of 10 parameters using only 14 rim configurations, see Table A1 in Appendix A and the correlating photos in Figure A1. This assumption was shown to be largely valid in the DPI, as detailed below. The last two configurations in Table

A1 (S13 and S14) were center points, used to determine the linearity of the parameter effects. The 11th screening parameter, the rim track design (No. 13), was evaluated separately with three specific profiles. Since no differences were found, this paper will not describe that part of the screening.

Detailed parameter investigation (2nd test session)

The literature survey together with the outcome of the screening tests resulted in 7 parameters to be investigated in detail. However, geometric restrictions prevented the study from including all parameters into one fractional factorial design (FFD) matrix. Therefore, three different FFD matrices were setup using five parameters in each matrix, see Table 3, meaning that each FFD would require 16 rim configurations, since 1st and 2nd order effects where investigated and higher order effects assumed negligible. Several parameters were a part of multiple FFD matrices, meaning that many rim configurations were duplicates and that the three FFD matrices could be acquired using only 32 unique rim configurations. Only 2nd order effects between parameters included in the same FFD matrix could be evaluated. An additional rim configuration (D41) was included to investigate the flowfield effects of various individual parameters. The combined test matrix can be seen in Appendix B, Table B1, along with photos of all configurations, see Figure B1.

Table 3. The included parameters in the three fractional factorial design setups.

No.	Name	FFD1	FFD2	FFD3
1	Coverage area	X	X	
2	Rim cover distance	X		X
3	Rim cover depth	X	X	X
4	Rim cover angle	X	X	X
6	Depth of center	X	X	X
7	Drop angle			X
11	Spoke window width		X	

Flowfield and pressure measurements

Wake Surveys

Wake surveys were conducted on test object 1 (sedan) at four Y-Z planes; Figure 1 shows the wind tunnel coordinate system. Figure 7 shows the four planes and the sampling points. Plane 1 was at the front right axle, plane 2 was 500mm behind the front right axle, plane 3 was 500mm upstream of the rear right axle, and plane 4 was 500mm downstream of the rear right axle. All planes started 25mm from the ground and stretched to 875mm high (Z-direction). All planes started 30mm from the tire (Y-direction); planes 1 and 2 extended to 380mm away from the tire, while planes 3 and 4 extended to 430mm away from the tire. Planes 3 and 4 were slightly wider to accommodate the growing wake.

The effects of three main rim geometric features on the flow field were investigated with the wake surveys; the coverage area (D36, D38, and completely covered with cover plates), the rim cover distance (D02 and D41), and the rim step, which is comprised of the rim cover depth and angle (D09 and D15). In addition to these geometric effects, the effects of having different front and rear rim designs were investigated by surveying the vehicle with F40R90, and F90R40. These two sets of surveys were only conducted at planes 2, 3, and 4 due to time restrictions.

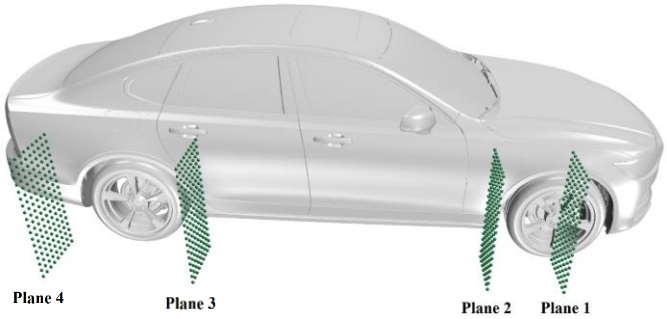

Figure 7: Position of wake planes taken around the S90. Grid points shown.

Two 12-hole omniprobes were used to traverse the wake planes at 50mm increments in both directions. The omniprobes accurately decomposed the pressures measured into the various flowfield parameters when the flow was within ±150° [22]. The omniprobes' spherical tips were 6.35mm in diameter. The flow was measured at each point for 5 seconds at a sampling rate of 1,000Hz. The data was acquired through a 24-bit Dewesoft Sirius HD STG-S module. The pressure sensors that were connected to the omniprobes were SensorTechnics HCLA0025DB.

From the wake surveys, the vorticity, total pressure coefficient, and local drag coefficient were calculated through Equations 1 to 3, respectively. It should be noted that the vorticity was calculated through the central difference scheme as it is a suitable trade-off between reducing the noise and reducing the smoothing of local maxima and minima.

$$\omega = \left(\frac{\partial w}{\partial y} - \frac{\partial v}{\partial z}\right) \quad (1)$$

$$C_{P_t} = \frac{1/2\,\rho V^2 + P_S}{1/2\,\rho {V_\infty}^2} \quad (2)$$

$$C_{D_L} = \left(1 - C_{P_t}\right) - \left(1 - \frac{u}{V_\infty}\right)^2 + \left(\frac{v}{V_\infty}\right)^2 + \left(\frac{w}{V_\infty}\right)^2 \quad (3)$$

Wheelhouse pressure measurements

The wheelhouse pressure measurements were taken in the front left wheelhousing at 40 points. The points were distributed in inside the wheelhouse and concentrated in areas where previous tests indicated interesting flow features. The locations of these points can be seen in Figure 8. The pressure sensors were the same as those used during the wake surveys, and connected to the same Data Acquisition System (DAQ), however, the measurements were taken at 5,000Hz for 5 seconds. These pressure measurements were then processed to give the average pressure coefficient and local drag coefficient from Equations 4 and 5, respectively. Equation 5 corresponds to the pressure measured in the wheelhouse decomposed into the drag direction (x-direction) through the arctangent of the angle between the resultant surface normal y- and z- components and the x-component of the surface normal vector. This value was then

multiplied by either +1 or -1 to account for the direction of the surface; i.e. so that a force in the positive direction was drag and a force in the negative direction was thrust.

Figure 8: Wheelhouse pressure sensor locations. Front left wheelhouse.

$$C_P = \frac{P - P_\infty}{1/2\,\rho {V_\infty}^2} \tag{4}$$

$$C_{D_L} = \frac{P \arctan\frac{\sqrt{y^2 + z^2}}{x}}{1/2\,\rho {V_\infty}^2} \tag{5}$$

Base Pressure Measurements

The base pressure measurements were taken with the same pressure sensors and DAQ as the wheelhouse and wake survey measurements. The measurements were taken at a 5000Hz sampling rate for 5 seconds. The averaged values were processed to give the pressure coefficient using Equation 4. The pressure sensors were located as shown in Figure 9 and were concentrated towards the edges of the vehicle where the highest pressure gradients were expected. The base drag was computed with the equation used by Landström, Löfdahl, and Walker [23]; Equation 6. The negative value in Equation 6 was incorporated to convert the value into the correct axis-system.

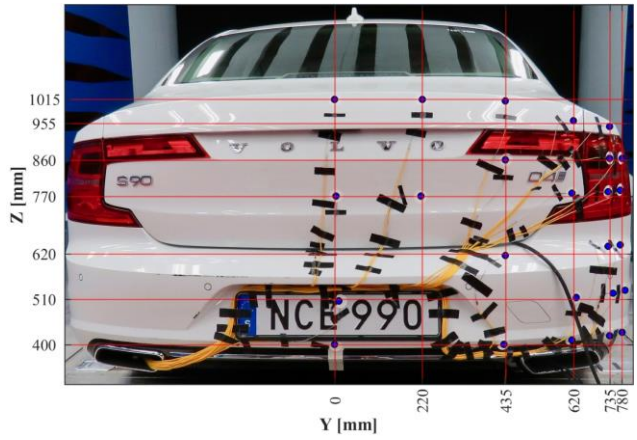

Figure 9: Location of wheelhouse base pressure sensors.

$$C_{D\,base} = -\frac{\sum_i C_{Pi} A_i}{A_{base}} \tag{6}$$

Numerical procedure

In addition to the experimental investigation, a numerical investigation was conducted on test object 1 (sedan) with rims D36 and D38.

A CFD model was developed. The geometry was cleaned and pre-processed in ANSA by BETA CAE Systems. The meshing, domain setup, simulation, and post-processing was done in STAR-CCM+ by Siemens.

Domain

The model's domain can be seen in Figure 10. The vehicle was placed one third of the distance from the inlet. The domain consisted of 280 million hexahedral (trimmed) cells. A boundary layer treatment mesh was applied on all surfaces; six layers of prism cells with a first cell height of 0.015mm was applied to all non-rotating surfaces, while eight layers with a first cell height of 0.01 mm was applied to the rotating surfaces. The y^+ was subsequently less than 1 and a minimum target cell size of 0.16mm. The mesh refinement zones can be seen in Figure 11.

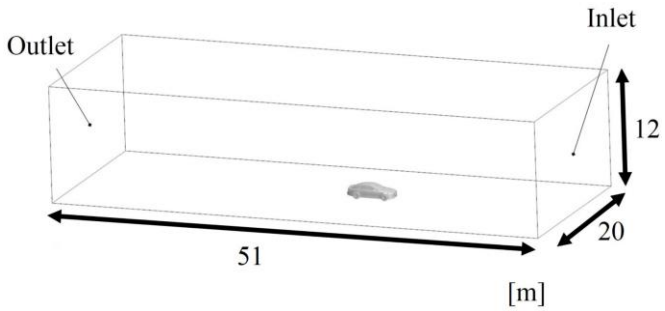

Figure 10: The numerical domain.

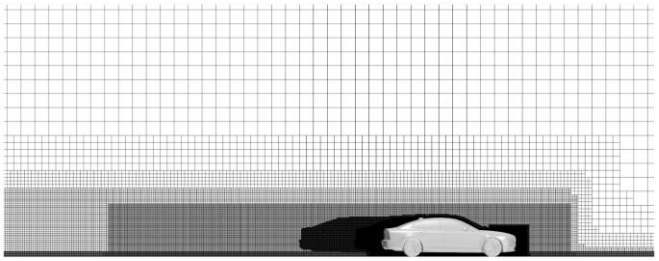

Figure 11. General mesh refinement zones around the vehicle.

Boundary conditions

The inlet was set to a velocity inlet with a normal velocity of 140km/h, while the outlet was set to a pressure outlet. The top and sides of the domain were set to symmetry planes, while the floor was set to a moving wall with the same tangential velocity as the inlet flow; 140km/h. The inlet's turbulence intensity was set to 0.001 to reflect the physical wind tunnel. All vehicle surfaces except the

wheels, the radiator, the A/C condenser, the charge air cooler (CAC), and the fan were set to no-slip.

Porous media

The pressure drops caused by the radiator, the A/C condenser, and the CAC were modelled in STAR-CCM+ by adding a source term, f_p, into the momentum transport equation [24], which accounted for the flow resistance of these parts with viscous and inertial terms measured from underhood components.

Rims and tires

In order to account for the wheel rotation, a sliding mesh, depicted in green in Figure 12, was applied to each wheel's rim, and a moving wall boundary condition was applied to each tire's surface. The sliding mesh region rotated with each time step. This rotation method precluded non-axisymmetric parts, therefore, the tire, which was not axisymmetric, could not be included in this region. The sliding mesh consisted of hexahedral cells with the same sizes as the outer domain. The cells at the interface between the sliding mesh region and the outer domain had a fixed size of 1mm on either side of the interface to ensure a smooth transition between the two domains.

In the experimental setup, the tires deformed due to the loading placed on them, and the rotational forces, which caused a radial expansion and an axial contraction [25]. Michelin© provided the authors with tire deformation geometries, which corresponded to the operating conditions used in the wind tunnel; rotating at 140 kph, loaded at Curb + 2, and cambered at 1°. It should be noted that Curb + 2 refers to the vehicle's curb weight with the driver and front passenger. These geometries were then incorporated into the numerical model. The deformed tire geometry supplied from Michelin© is shown in Figure 12. The tires could be supplied with the rotationally axisymmetric rain grooves, but not with lateral grooves.

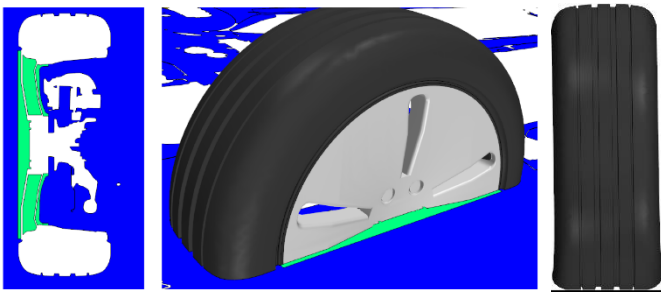

Figure 12: The sliding mesh setup; sliding mesh domain (green). A cross-sectional view of the front left wheel is on the left, and a perspective view of the front left wheel is in the middle. The deformed tire geometry from Michelin© is on the right.

Solver setup

An IDDES turbulence model was employed, with a 2nd- order temporal discretization and a timestep of 5 x 10^{-4} seconds.

The model was solved for a total of six seconds, with the last three seconds incorporating rotation of the wheel, and the drag coefficient calculated by averaging this value over the last two seconds of the simulation. Hobeika and Sebben [26] showed that increasing this averaging time does not significantly affect the drag coefficient.

Results

The results are divided into three parts; the experimental force measurements, the experimental flowfield measurements and the CFD simulations. The flowfield and CFD results are used to further explain the force measurement results.

Force measurements

Most of the force measurement results were obtained from the regression model developed from the DPI data. Interesting results were also found during the screening and the separate evaluation of the coverage area. All of those results were, however, dependent on the validity of the modular wheel concept.

Validation of the modular wheel concept

The results of the validation can be seen in Table 4. The validation was done by comparing a real PW to the same rim geometry created by the modular wheel concept (S19). Since tires from different manufacturing batches were mounted on the PW and the BW, these differences in the drag coefficient caused by these different batches were isolated by comparing the drag results when having cover plates mounted onto the wheels. The tire batch differences where -2 and -1 drag counts (ΔC_D = -0.002 & -0.001) for open and closed cooling flow, respectively. These differences were then considered when comparing S19 to the PW, resulting in a $\Delta\Delta C_D$ of 1 count for open cooling and 2 counts for close cooling. The modular wheel concept was therefore regarded valid, since the differences were small and close to the uncertainties of the wind tunnel itself, see Table 1.

Table 4. The difference between the base wheel and the production wheel when using cover plates (to determine the effect of the different tire batches on the drag coefficient), along with the difference between the production wheel and the representation of the production wheel (S19) using the modular wheel concept. As a result, the difference in drag between the production wheel and S19 are isolated.

Cooling flow	*Cover plates* **BW – PW** ΔC_D	**S19 – PW** ΔC_D	$\Delta\Delta C_D$
Open	-0.002	-0.001	0.001
Closed	-0.001	0.001	0.002

Coverage area

The coverage area was the rim design parameter with the greatest influence on the aerodynamic drag. Three rim configurations, see Figure 5, were compared to the reference of a fully covered wheel (100 % coverage area), see Figure 13. The parameter was found to have a linear effect on the aerodynamic drag.

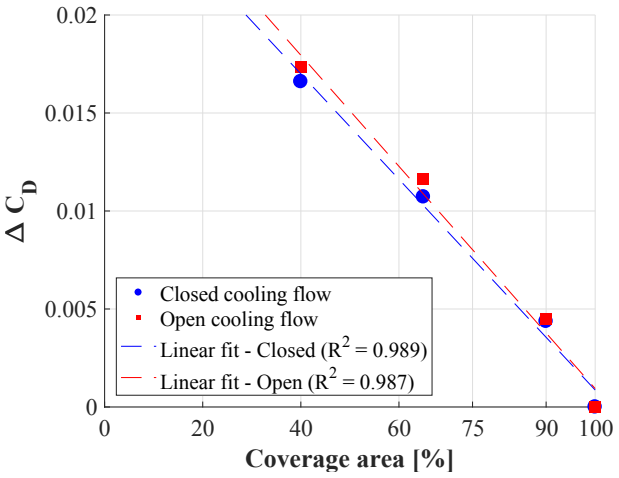

Figure 13. The isolated effect of the coverage area on the aerodynamic drag, for both open and closed cooling flow. Linear fit models are also shown.

Different front and rear rims

Table 5 shows the effects on the drag coefficient when changing the front and rear rims independently and at the same time from the 40 % to the 90 % covered rim (D36 to D38). Summating the drag reduction from the independent changes results in the total reduction when changing the front and the rear wheels at the same time. This occurs for both open and closed cooling flow, hence no aerodynamic drag synergy between the front and rear rims was found.

Table 5. The change in the drag coefficient among the different front and rear rims. The D36 (40 % covered) rim was used as the reference drag coefficient for both the open and closed cooling configurations.

Cooling flow	Front rims	Rear rims	ΔCd
Open	D36 (40 %)	D36 (40 %)	Ref.
Open	D36 (40 %)	D38 (90 %)	-8
Open	D38 (90 %)	D36 (40 %)	-4
Open	D38 (90 %)	D38 (90 %)	-12

Closed	D36 (40 %)	D36 (40 %)	Ref.
Closed	D36 (40 %)	D38 (90 %)	-8
Closed	D38 (90 %)	D36 (40 %)	-5
Closed	D38 (90 %)	D38 (90 %)	-13

Screening

The screening tests resulted in a ranking of significance, based on the aerodynamic drag, see Figure 14. Similar results were found with open cooling flow. A high standardized effect indicates that it is extremely unlikely that the parameter does not have an influence on the aerodynamic drag. The red dashed vertical line displays the significance limit (based on a *p*-value of 0.05). Therefore, the study found that the bottom three parameters (No. 5, 12 and 9) were insignificant and did not affect the drag. No. 4, 6, 3 and 11 had the highest standardized effects and were selected for closer evaluation in the DPI. The rest, parameters No. 10, 8 and 14, were not analyzed further due limited resources.

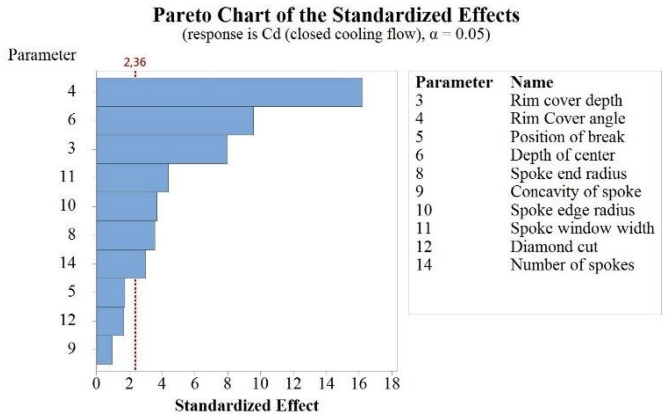

Figure 14. Pareto chart indicating the significance of the parameters included in the screening, for closed cooling flow. The red dashed line represents the level of significance corresponding to a *p*-value of 0.05.

Detailed parameter investigation

The detailed parameter investigation setup enabled an analysis of the parameters' 1st and 2nd order effects. The significance of the parameters' effects was evaluated, as in the screening. The significant parameters were then used in a linear regression model to predict the aerodynamic drag by altering the parameter levels. The predicted C_D values were compared to the measured values, see Figure 15. The largest residual was only 2 drag counts from its measured value, and 95 % of the predicted configurations were within ±1.82 counts of the measured value (almost to the uncertainty level of the wind tunnel). The model was considered accurate with a R^2 fit above 0.93. However, this was when testing the model on the data which the model was based. The model could potentially differ more when predicting other rim geometries not included in this study.

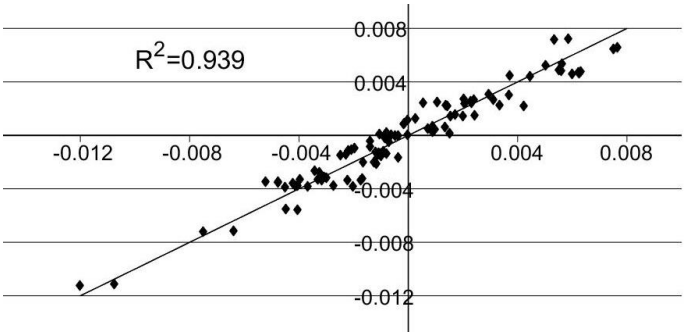

Figure 15. Measured vs. predicted ΔC_D for all configurations (including open and closed cooling flow) based on the regression model. The reference at the origin represent the center point D33.

However, the regression model in this study was primarily used to gain knowledge on the most important 1st and 2nd order parameter effects, see Figure 16. The aerodynamic drag effects when changing from a geometric minimum to a maximum value are displayed for the significant parameters in the regression model. Six parameters were found to have a significant effect on the drag for test object 1 (sedan) and test object 2 (estate), see Figure 16. Only two 2nd order synergy effects between parameters No. 2 & 4 and No. 3 & 4 were significant and they were all related to the same geometric region (the rim cover).

It was evident that the coverage area (No. 1) had the highest influence on the drag. However, it was not the only important parameter. The rim cover distance (No. 2) was found to have a low effect but was used in the regression model since it was part of a synergy with the rim cover angle (No. 4). Both the rim cover depth (No. 3) and angle (No. 4), which caused a geometric step between the top surface of the spoke and the rim cover, had a significant effect. Likewise, the depth of center (No. 6) and the drop angle (No. 7) were significant. Figure 16 shows that the same trends could be seen regardless of the vehicle type, except for the rim cover angle (No. 4), which was insignificant for test object 2. The largest difference in magnitude was found for the coverage area, where it had a smaller effect on the aerodynamic drag for an estate type vehicle.

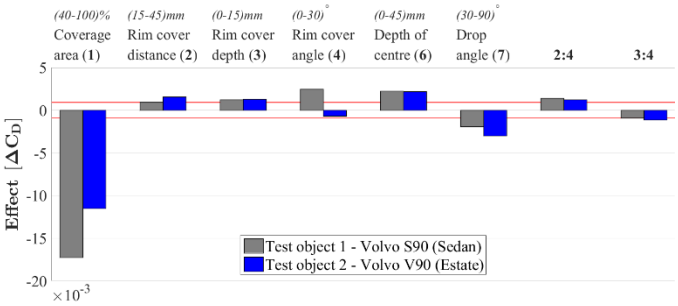

Figure 16. The magnitude of the significant rim parameter effects, for a sedan and estate vehicle. **2:4** and **3:4** represent the 2nd order effects between the numbered parameters, and the vertical red lines indicate the significance limit.

The study of test object 1 found that the cooling flow setting did not have any synergy with the rim geometry, meaning that a fixed adjustment value could be used to predict the difference between open and closed cooling flow, see Figure 17. This model was accurate with a R^2 value above 0.98, the largest residual was only 1 drag count from its measured value, and 95 % of the predicted configurations were within ±0.96 counts of the measured values, meaning that the model had the same uncertainty as the wind tunnel.

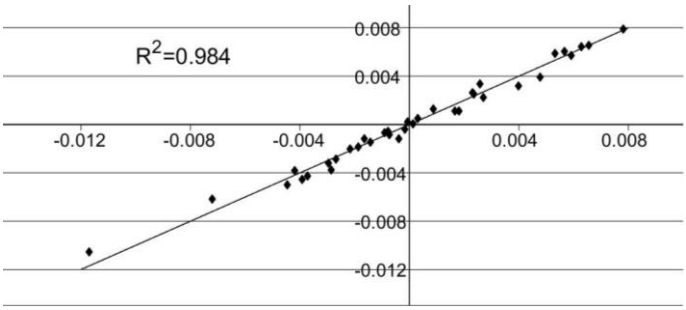

Figure 17. The measured vs. predicted ΔC_D of the closed cooling flow results, based on the fixed adjustment subtracted from the open cooling flow results of the same configuration. The reference at the origin represents the center point D33.

Flowfield

The results presented herein pertain to the coverage area, the rim cover depth, the rim cover angle, the synergy between the rim cover distance and the rim cover angle, the synergy between the rim cover depth and the rim cover angle, and the effects of different front and rear rims.

Coverage area

The DPI identified that, the rim coverage area greatly affects the vehicle's drag. It was also identified that; the drag of the vehicle is inversely proportional to this parameter. As such, wake surveys, base pressure measurements, and wheelhouse pressure measurements were conducted on three rim types of various coverage area; completely covered, 90% covered (D38), and 40% covered (D36). Figures 18 to 20 show the vorticity plots and base pressure coefficients of these three configurations with closed cooling, respectively. The wake survey plots are ordered such that the closest plot to the vehicle corresponds to plane 1, and each subsequent plane to the right corresponds to the next plane downstream. Figures 21 to 23 show the local drag coefficient plots and base pressure coefficients. It should be noted that the total pressure coefficients are not presented for brevity as they largely reflect Figures 21 to 23. It should also be noted that the regions with a total pressure coefficient less than zero in planes 1 and 2 correspond to the regions of highest local drag coefficient, while no regions in planes 3 and 4 had total pressure coefficients less than zero.

One of the most obvious effects of the coverage area is its effect on the near-ground jetting vortex; the completely covered rim does not exhibit an obvious jetting vortex in planes 1 and 2, with positive and negative vorticity regions persisting downstream. D38 shows almost no vorticity associated with a vortex in this region. D36 shows high positive vorticity in this region, which is indicative of the typical jetting vortex. In addition, looking at the direction of the flow in the jetting vortex region shows that for the completely covered wheel, the flow is towards the wheel. As the rim becomes more open, the flow is directed away from the wheel, as shown by the arrows, indicating that more air is flowing through the rim and feeding the jetting vortex. These effects are reflected in the local drag coefficient plots, where there is a lower drag in the jetting vortex region of the completely covered and D38 rims. These effects will be further elaborated on in the numerical results section.

In planes 2 and 3, all three rims exhibit similar upper vortex structures and flow directions. However, as the rim becomes more covered, the middle region (at approximately 0.4m above the ground) produces a higher local drag coefficient, and the upper region (at approximately 0.6m) reduces in drag.

There is little difference in plane 3's vorticity, indicating that the varied effects of the coverage area found upstream have dissipated. However, as the coverage area increases, the local drag coefficient plot becomes less triangular and more semi-circular; there is less loss around the contact patch and jetting vortex regions and more loss at the center of the rim.

The coverage area has a similar effect on the rear wheel jetting vortex, as seen in plane 4 where the completely covered and D38 rims do not increase the near ground vorticity, while D36 does. This is also reflected in the local drag coefficient plots, where D36 exhibits greater loss in the lower region of the plane than the other two rims. Furthermore, the completely covered and D38 rims experience higher loss in the middle of the rim, which is consistent with the upstream plane effects. This explains why the D36 local drag coefficient plots in planes 3 and 4 are triangular, while the D38 plots are more circular. The remainder of the vortex structures in plane 4 are relatively unchanged.

The rim coverage area also affects the base pressure coefficient of the vehicle; the pressure coefficient increases with increasing coverage area in the middle of the base, most notably in the middle, and towards the sides of the base. Increasing the coverage area from 40 % (D36) to 90 % (D38) reduced the base drag coefficient with 3.1 and 1.9 counts for closed and open cooling flow, respectively.

Additionally, pressures in the front left wheelhouse were taken for these three configurations. Figure 24 shows the pressure coefficient distributions of the three rims, while Figure 25 shows the local drag coefficient distributions. Completely covering the rim results in a lower pressure region forming in the downstream outer edge of the housing. This low pressure region does not occur for either of the other two rim configurations. The D36 rim features a low pressure, and subsequently a higher local drag coefficient, on the upstream face, whereas the D38 rim features a high pressure in this region; the completely covered rim exhibits a pressure, and local drag coefficient, between these two extremes. Similar effects occur with open cooling.

Figure 26 shows the average local drag coefficient of each plane of the wake surveys, and shows that the D38 configuration has the lowest average local drag coefficient for planes 1 and 2, and from plane 3 onwards, the average local drag coefficient of each rim assumes the expected order in relation to each other. Therefore, under certain conditions it may be better to have D38 front rims instead of completely covered, however, further investigation into the downstream effects is required.

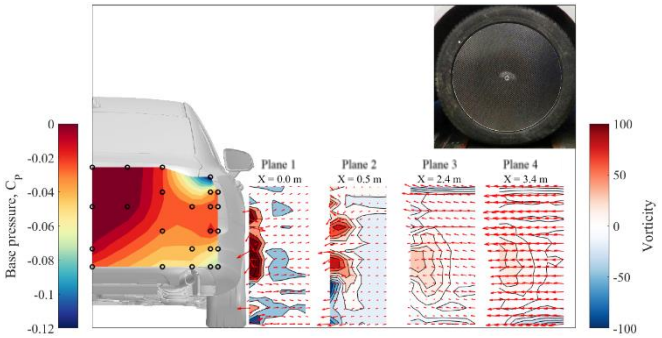

Figure 18. Vorticity and base pressure of completely covered rim. Closed cooling.

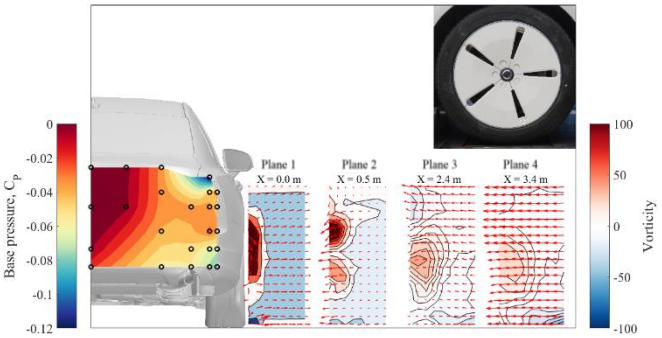

Figure 19. Vorticity and base pressure of D38 (90% coverage area) rim. Closed cooling.

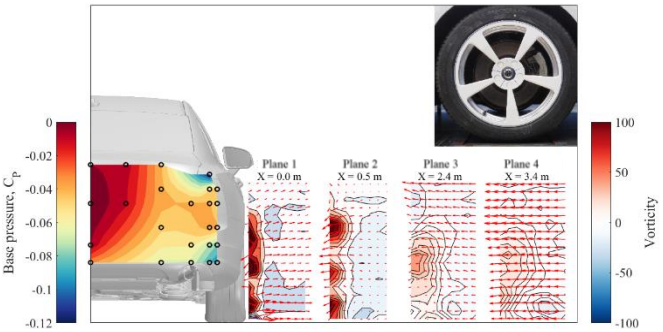

Figure 20. Vorticity and base pressure of D36 (40% coverage area) rim. Closed cooling.

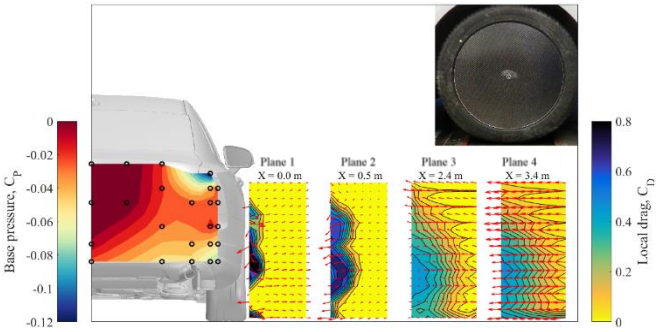

Figure 21. Local drag coefficient and base pressure of completely covered rim. Closed cooling.

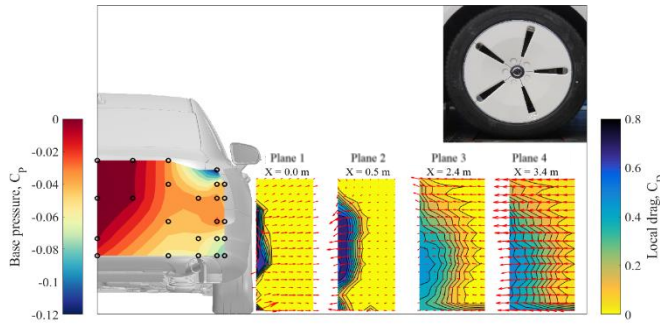

Figure 22. Local drag coefficient and base pressure of D38 (90% coverage area) rim. Closed cooling.

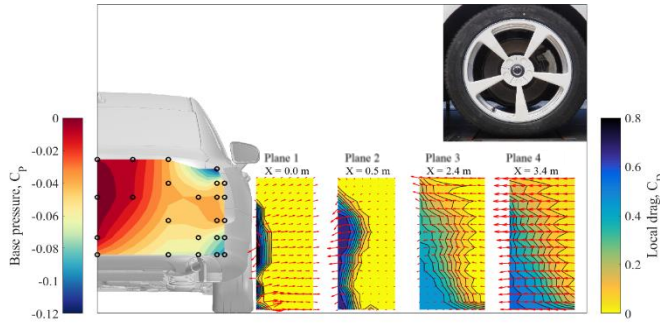

Figure 23. Local drag coefficient and base pressure of D36 (40% coverage area) rim. Closed cooling.

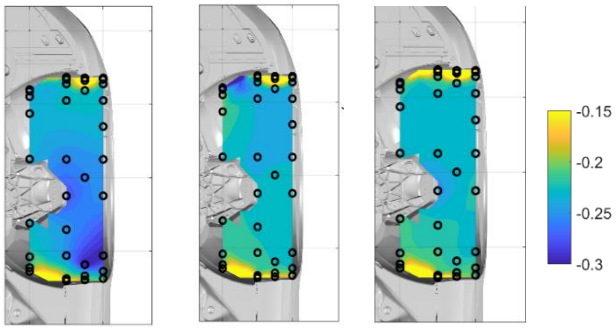

Figure 24. Front left wheelhouse pressure coefficient distribution of the Completely covered (left), D38 (middle), and D36 (right) configurations with closed cooling.

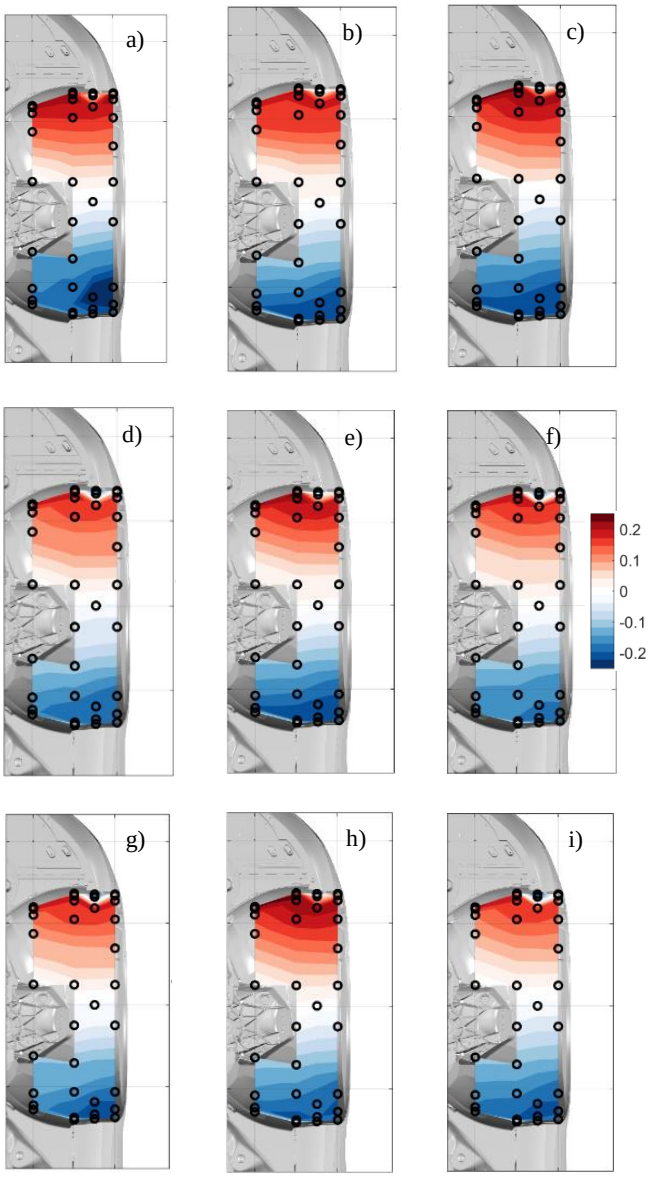

Figure 25. Front left wheelhouse local drag coefficient distribution of the Completely covered CC (a), D38 CC (b), D36 CC (c), D14 OC (d), D01 CC (e), D01 OC (f), D41 OC (g), D13 CC (h), D13 CC (i) configurations.

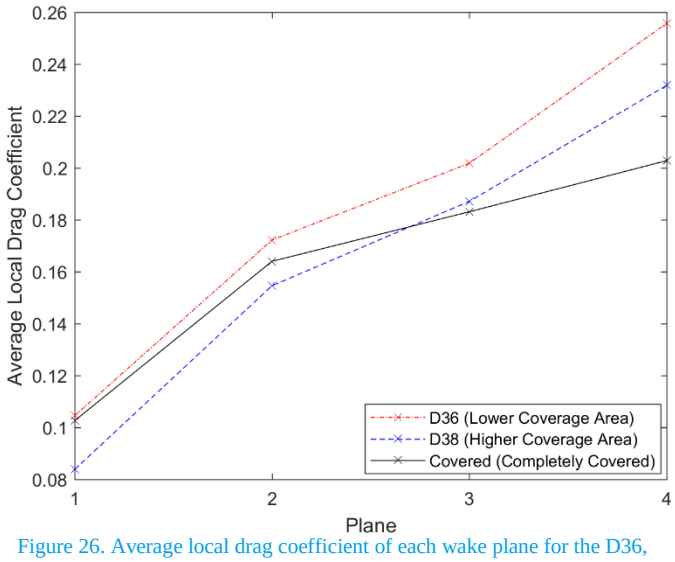

Figure 26. Average local drag coefficient of each wake plane for the D36, D38 and completely covered rims.

Rim cover depth

Comparing rims D12 to D41 gives the direct isolated effects of reducing the rim cover depth. The force measurements presented above shows that the rim cover depth had no effect on the drag coefficient, regardless of the cooling flow configuration. However, Figure 27 shows that reducing the rim cover depth increases the pressure coefficient in the upper half of the base area, especially at the upper corners. The pressure coefficient in the lower third is increased, especially around the lower corners. Similar patterns were seen for both open and closed cooling configurations. Reducing the rim cover depth with closed and open cooling reduces the base drag coefficient by 1.9 and 1.6 counts, respectively.

The wheelhouses exhibited little difference in the pressure coefficient and the local drag coefficient. Therefore, the plots are omitted.

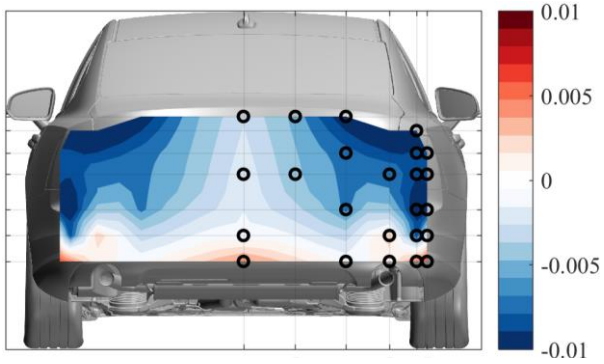

Figure 27. Base pressure of the D12 rim minus D41 rim with closed cooling. Negative indicates that the former rim had a lower pressure coefficient.

Rim cover angle

Comparing the geometries of the D14 and D41 rims shows that reducing the rim cover angle results in a 3 and 2 count reduction in the drag coefficient with closed and open cooling, respectively. Figure 28 shows that reducing the rim cover angle with closed cooling greatly increases the base pressure coefficient over the majority of the base area, and a 4.6 count reduction in the base drag coefficient occurs, which reflects the overall drag coefficient change when reducing the rim cover angle. Figure 29 shows that, reducing the rim cover angle with an open cooling configuration still increases the pressure coefficient over the majority of the base area, but to a lesser extent. In addition, it slightly increases it in the lower corners. Overall, reducing the rim cover angle with open cooling reduces the base drag coefficient by 1.4 counts.

There is little difference between the closed cooling D14 and D41 wheelhouse pressure and local drag coefficient plots, therefore, they are omitted. Figure 25 shows the wheelhouse local drag coefficient distribution of the D14 and D41 rims with open cooling. Reducing the Rim Cover Angle results in a lower local drag coefficient on the downstream face, which would contribute to the overall drag coefficient reduction caused by reducing this feature.

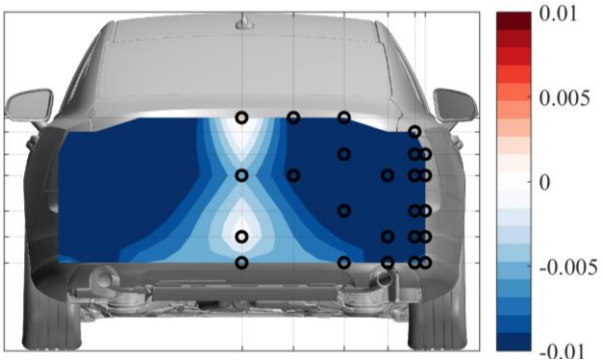

Figure 28. Base pressure of the D14 rim minus D41 rim with closed cooling. Negative indicates that the former rim had a lower pressure coefficient.

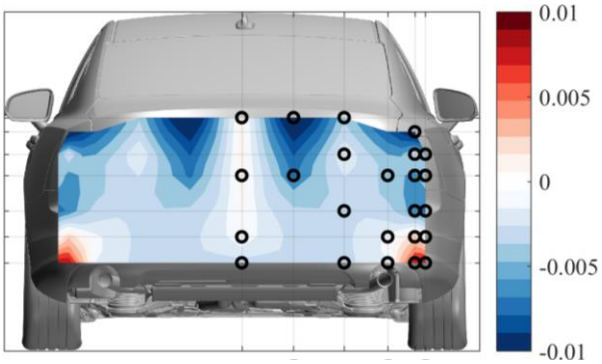

Figure 29. Base pressure of the D14 rim minus D41 rim with open cooling. Negative indicates that the former rim had a lower pressure coefficient.

Rim cover distance & rim cover angle

The DPI analysis presented above showed that there is significant synergy between the rim cover distance and the rim cover angle. Rims D01 and D13 demonstrate the effects of changing these two parameters together; D13, which has the higher values for these parameters, produces a 7 count greater drag than the D01 configuration, regardless of the cooling configuration.

Figure 30 shows the change in the base pressure distribution between the D01 and D13 rims with closed cooling. Increasing the rim cover distance and rim cover angle reduces the pressure coefficient over almost the entire base area, which results in a 3.3 count increase in the base drag coefficient. With open cooling, as shown in Figure 31, increasing these parameters slightly increases the pressure coefficient in the upper region of the base while reducing it in the lower region. Overall, no change in the base drag coefficient occurs.

Increasing the rim cover distance and rim cover angle with closed cooling increases the local drag coefficient on the upstream and downstream faces of the wheelhouse, as shown in Figure 25 e) and h). With open cooling, increasing these parameters reduces the local drag coefficient on the downstream face (Figure 25 f) and i)).

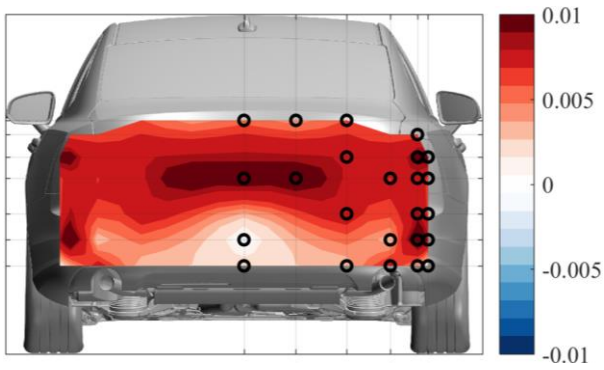

Figure 30. Base pressure of the D01 rim minus D13 rim with closed cooling. Negative indicates that the former rim had a lower pressure coefficient.

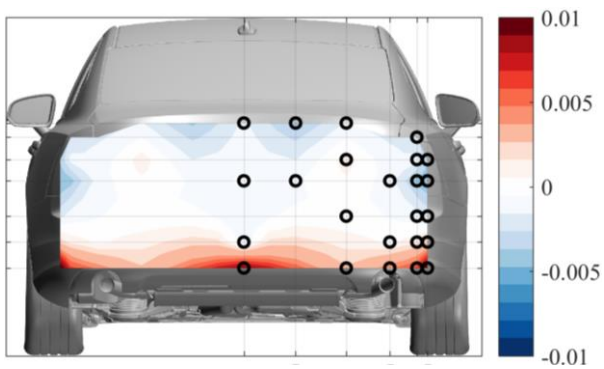

Figure 31. Base pressure of the D01 rim minus D13 rim with open cooling. Negative indicates that the former rim had a lower pressure coefficient.

Rim cover depth & rim cover angle

The results from the DPI showed that a synergy occurred between the rim cover depth and rim cover angle. Increasing both of these parameters results in a step between the top surface of the spoke and the rim cover forming. Comparing D09 and D15 geometries shows that D15 has a greater rim cover depth and a greater rim cover angle. This feature results in a 6 and 7 count drag coefficient increase with open and closed cooling, respectively.

Figures 32 and 33 show the vorticity wake planes of D09 and D15 with closed cooling, respectively. Figures 34 and 35 show the local drag coefficient plots of D09 and D15 with closed cooling, respectively. The total pressure coefficient plots are not included as they largely reflect the local drag coefficient plots. In all planes, incorporating the step results in a greater vorticity in the near-ground jetting vortex region, which results in a greater local drag coefficient. This subsequently makes the local drag coefficient plots more triangular in planes 3 and 4. Therefore, the rim cover step appears to have a similar effect on the jetting vortex as the coverage area; incorporating the rim cover step promotes more flow exiting through the rim and feeds the jetting vortex. The upper region's vorticity and local drag coefficient distributions are relatively unaffected by the step.

Figure 36 shows the base pressure coefficient distribution of the D09 and D15 rims, with closed cooling. The D09 rims produce a higher pressure coefficient over most of the base area than the D15 rims, which results in a 2.5 count lower base drag coefficient. The base pressure distributions approximate each other with open cooling.

The wheelhouses exhibited little difference in the pressure coefficient and local drag. Therefore, the plots are omitted. The pressure coefficient plots are not included as they largely reflect the local drag coefficient plots.

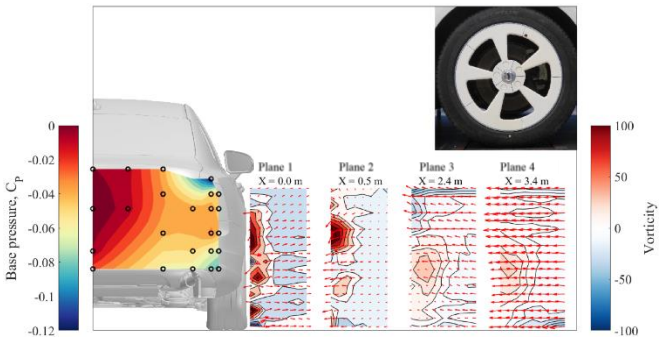

Figure 32. Vorticity of D09 rim. Closed cooling.

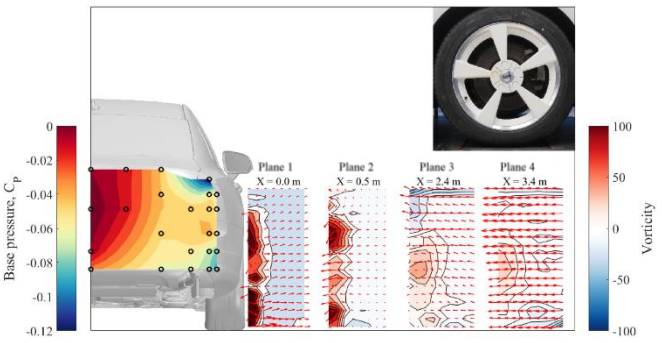

Figure 33. Vorticity of D15 rim. Closed cooling.

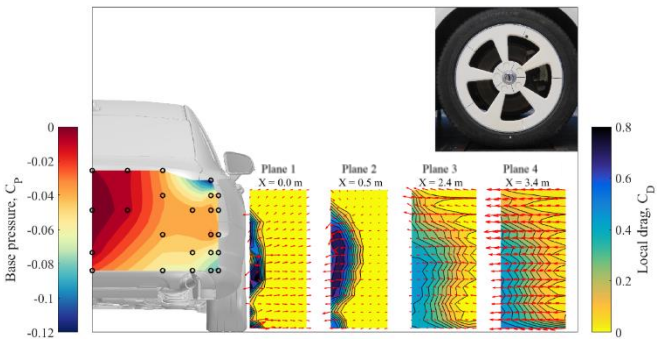

Figure 34. Local drag coefficient and base pressure of D09 rim. Closed cooling.

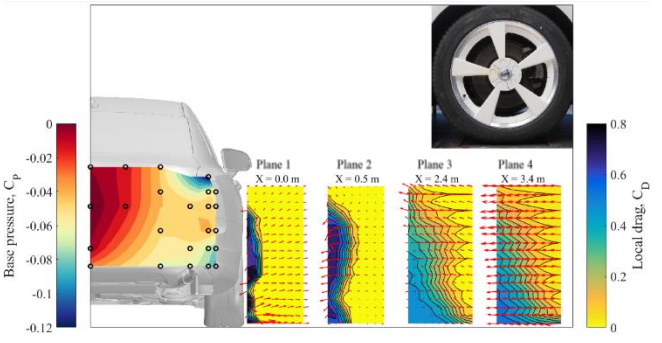

Figure 35. Local drag coefficient and base pressure of D15 rim. Closed cooling.

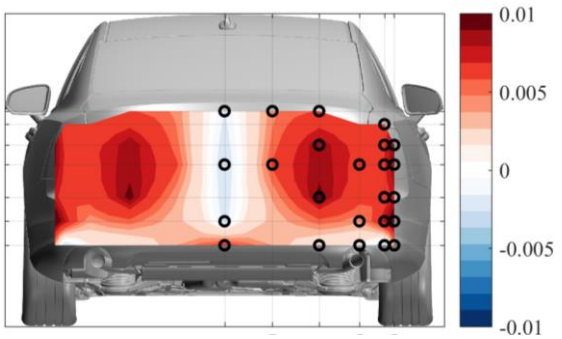

Figure 36. Base pressure change, D09 rim minus D15 rim with closed cooling. Negative indicates that the former rim had a lower pressure coefficient.

Different front and rear rims

Figure 37 shows the change in the local drag coefficient at planes 2, 3, and 4 between various configurations in Table 6. The changes in the vorticity and total pressure coefficient largely reflect the local drag coefficient distributions, and hence are omitted for brevity.

Table 6. The rim geometries of the configurations used to investigate the effects of different front and rear rims on the drag coefficient and flow field.

	Front rims	Rear rims
Configuration 1	D36 (40 %)	D36 (40 %)
Configuration 2	D36 (40 %)	D38 (90 %)
Configuration 3	D38 (90 %)	D36 (40 %)
Configuration 4	D38 (90 %)	D38 (90 %)

The local drag coefficient plots in plane 2 show that having the same front rims and different rear rims (config. 1 – config. 2, and config. 4 – config. 3) gives very similar distributions. Expectedly, having different front rims and the same rear rims (config. 1 – config. 3, and config. 4 – config. 2) yields almost the same change in magnitude in the local drag coefficient as having different rims on the front and rear wheels (config. 1 – config. 4).

In plane 3, having the same front rims and different rear rims (config. 1 – config. 2, and config. 4 – config. 3) still yields more similar local drag coefficient distributions than having the same rear rims and different front rims (config. 1 – config. 3, and config. 4 – config. 2), despite this plane being at the start of the rear wheels.

Surprisingly, in plane 4, having the same front rims and different rear rims (config. 1 – config. 2, and config. 4 – config. 3) still yields more similar local drag coefficient plots than having different front rims and the same rear rims (config. 1 – config. 3, and config. 4 – config. 2). Therefore, the front rims appear to dominate the flow field development down the side of the vehicle.

It should be noted that no base or wheelhouse pressure measurements were taken for these rim configurations.

The force measurements detailed that both the front and rear rims affect the drag coefficient, therefore, while the front rims dominate the flow fields surveyed, it is concluded that the rear rims affect other regions in the flow – most likely the base of the vehicle.

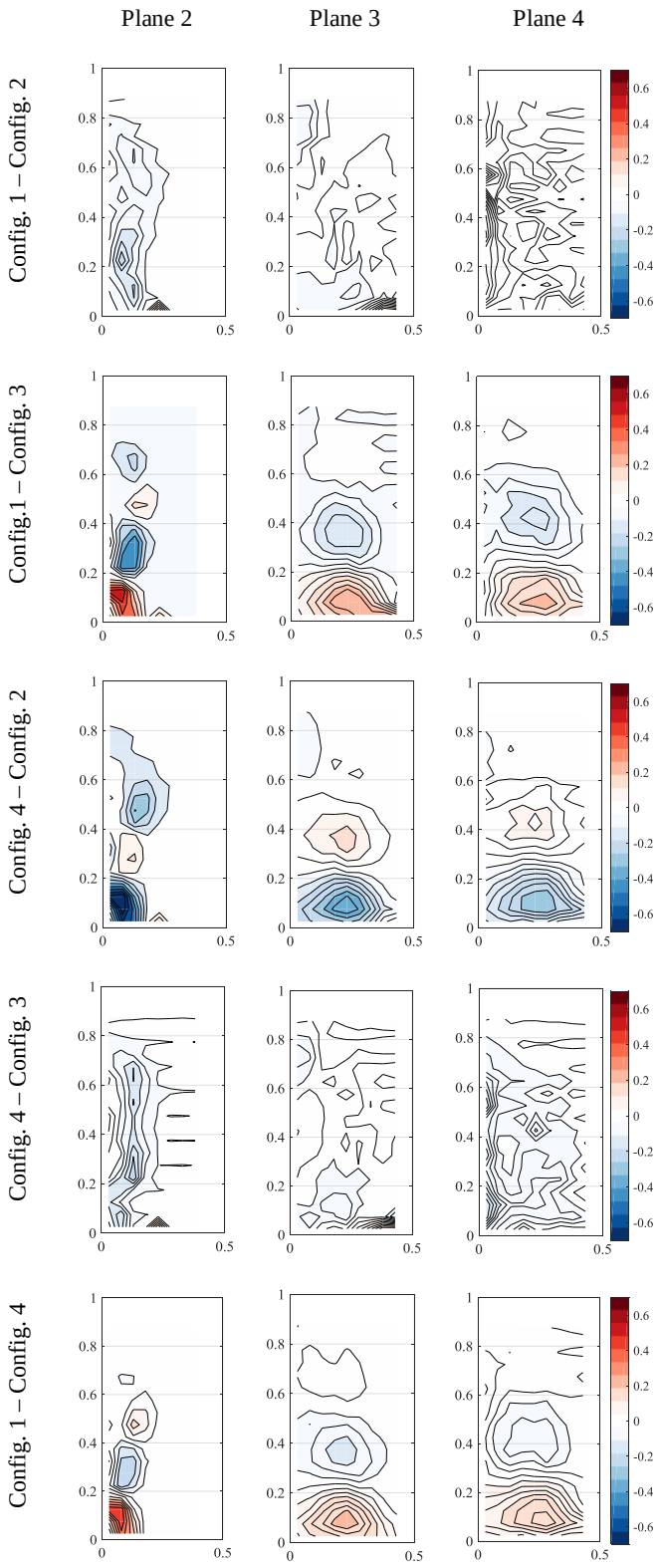

Figure 37. Changes in the local drag coefficient between various configurations at planes 2, 3, and 4. Closed cooling.

CFD

Validation

The CFD model was validated against the experimental results and the results can be seen in Table 7. The more open rim was slightly better predicted, however, both rims with both cooling configurations were fairly-well predicted; the errors from the simulations were significantly smaller than the changes in the drag coefficient caused by changing the rim coverage area. In addition to the drag coefficients, the flowfield measurements were used to further validate the CFD model. Figure 38 shows the CFD model and the experimental total pressure coefficient distributions with the D36 rim with closed cooling (using the experimental sampling point grids). In all planes, the CFD model closely resembles the experimental results. Figure 39 shows the CFD model and the experimental total pressure coefficient distributions with the D38 rim with closed cooling. The first and second CFD planes closely resemble the experimental results, which correspond to the front wheel. However, the model becomes dissimilar at planes 3 and 4, which correspond to the rear wheel. The vorticity distribution from the CFD simulation can be found in Appendix C. Figure C1 shows the D36 vorticity distributions from the CFD model. As the vorticity is calculated through the spatial derivatives of the crossflow-velocities, the errors are expected to magnify, however, there is still good agreement in all planes for the D36 rim between the CFD and the experiments (Figures 20 and C1). Figure C2 shows the D38 vorticity distributions of the CFD simulation; the first two planes show good similarity to the experiments (Figure 19), however, expectedly, the last two planes, which focus around the rear wheel, begin to lose this similarity. Therefore, only flow at the front wheel was analysed in the additional CFD analysis.

Table 7. Comparison of experimental drag coefficient results with the CFD simulation drag coefficients. D36 rim has a 40% coverage area, while D38 had a 90% coverage area.

	D36		D38	
	Exp.	**CFD**	**Exp.**	**CFD**
ΔC_D (Open)	Ref.	-0.004	Ref.	-0.006
ΔC_D (Closed)	Ref.	-0.004	Ref.	-0.007

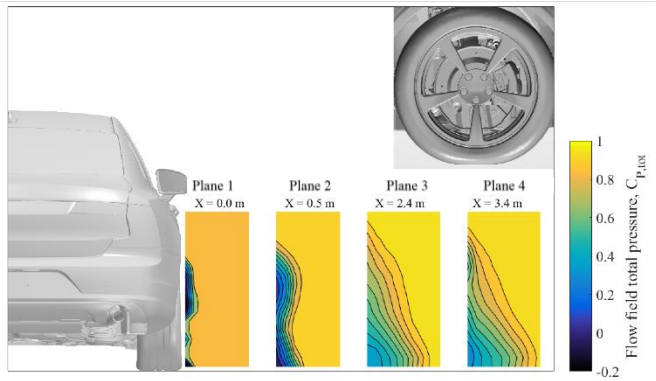

(a) CFD solution.

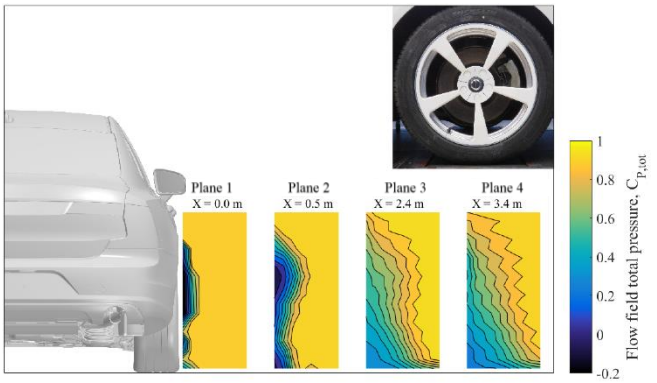

(b) Wind tunnel experiments.

Figure 38. Comparison of the CFD model, a), and experimental, b), total pressure coefficient distributions of the D36 rim with closed cooling.

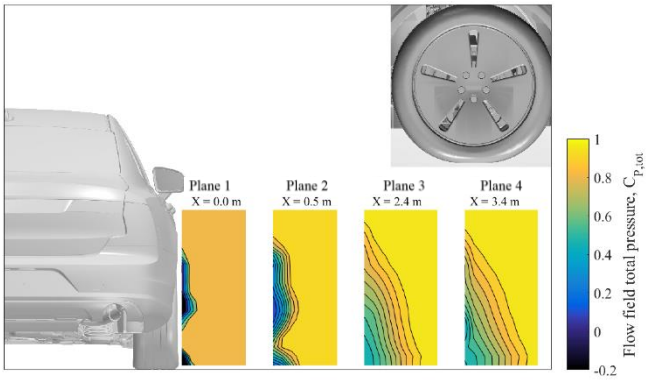

(a) CFD solution.

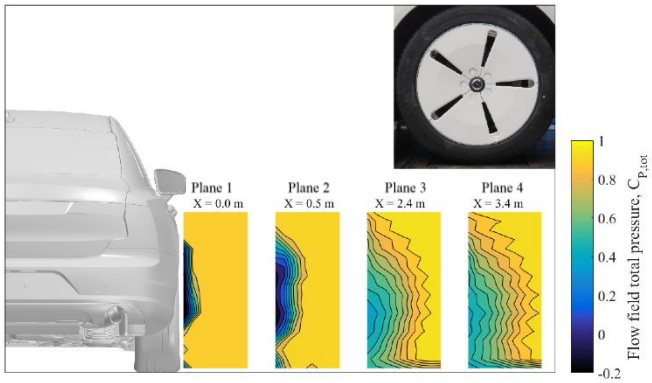

(b) Wind tunnel experiments.

Figure 39. Comparison of the CFD model, a), and experimental, b), total pressure coefficient distributions of the D38 rim with closed cooling.

Additional Numerical Analysis

Figure 40 shows the lateral flow velocity (v) around the front wheel at a plane 10 mm away from the vehicle of the D36 and D38 rims with closed cooling. There is significantly greater magnitude at the lower-rear of the D36 rim than the D38 rim, which shows more fluid flowing through the rim into the jetting vortex zone. This agrees with the experimental results and shows how the rim configuration can feed the jetting vortex and affect the drag production associated with it. Alternatively, there is more fluid exiting the top-rear part of the wheelhouse of the D38 wheel than the D36 wheel, correlation with the low pressure region seen in Figure 24 for the fully covered rim.

Figure 41 shows the vertical flow velocity (w) around the front at a plane 10 mm away from the vehicle of the D36 and D38 rims with closed cooling. The main difference occurs at the rear of the rims, where the D36 rim has a greater upwards velocity than the D38 rim. There is a slight difference in the upwards velocity at the lower-front of the wheel.

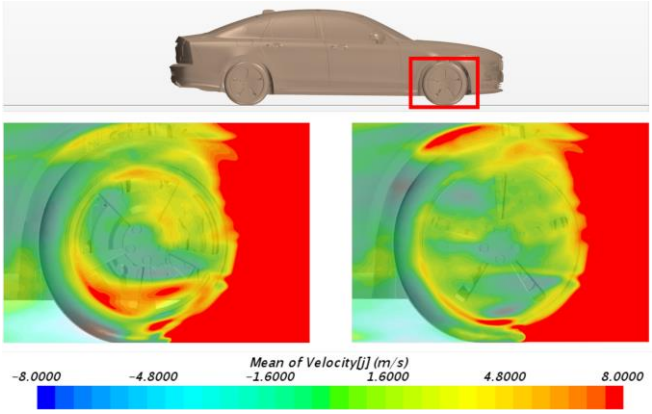

Figure 40. The mean lateral velocity (v) around the front wheel at a plane 10 mm from the vehicle of the D36 rim (left) and D38 rim (right). Red indicates flow out of the page, and blue indicates flow into the page. Closed cooling.

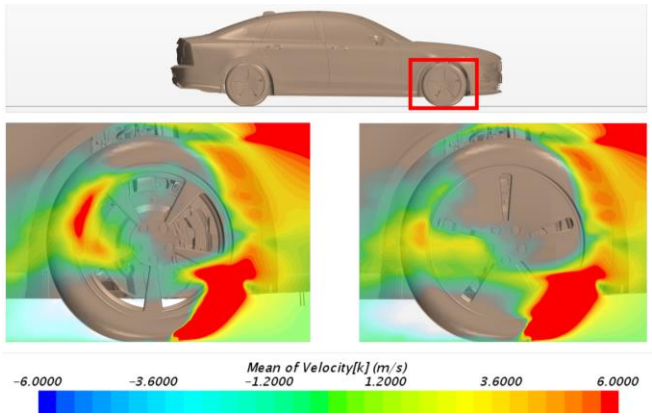

Figure 41. The mean vertical velocity (w) around the front wheel at a plane 10 mm from the vehicle of the D36 rim (left) and D38 rim (right). Red indicates flow moving upwards, and blue indicates flow moving downwards. Closed cooling.

Figure 42 shows the mean streamwise vorticity (u) around the front wheel at a plane 10 mm from the vehicle. It shows the D36 and D38 rims with closed cooling. The differences in the lateral and vertical velocities noted above manifest themselves as differences in the streamwise vorticity, where differences between these two rims occur in the lower-rear of the rim, top-rear of the wheelhouse, the rear of the rims, and the lower-front of the wheel. In other words, the differences in these velocities consequently affect the vortex production and breakdown. The vortex exiting the upper part of the wheel house was more distinct and longer-lasting for the D38 rim, indicating a stronger vortex.

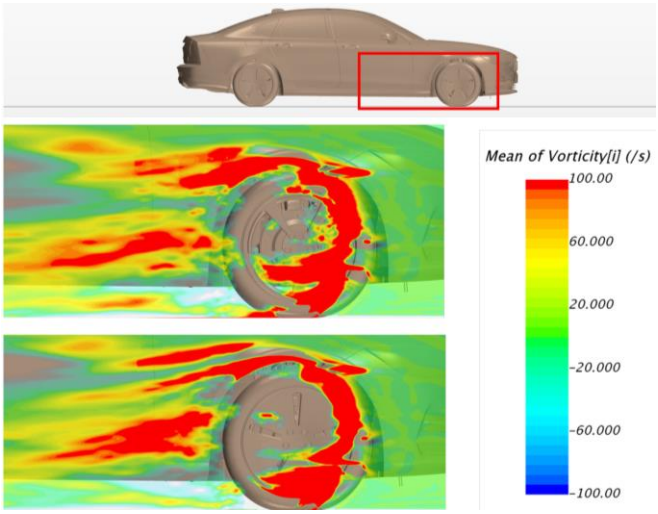

Figure 42. The mean streamwise vorticity (u) around the front wheel at a plane 10 mm from the vehicle of the D36 rim (middle) and D38 rim (bottom). Closed cooling.

Robustness of results

It was already shown that the general trends found were applicable to different vehicle geometries using the same setup. A potential difference to the setup include allowing the vehicle to "float" instead of having the ride height fixed. This change in setup would alter the positions of the wheels inside the wheelhousings. While these differences may alter the exact change in the drag coefficient caused by the different rim parameters, the trends are not expected to change significantly, as other studies have detailed similar effects to some of those found in this study [6, 8, 15, 27]. These studies used different vehicles, and thereby different wheelhouse packing and ride heights.

The applicability of the results presented above to wind tunnels with different moving ground systems is of interest. Gleason *et al.* [15] investigated the effects of covering a rim using a single belt moving ground system, while Bolzon *et al.* [28] investigated several rim parameters detailed above on a 1/5th scale vehicle with rotating wheels. The effects of the rim parameters investigated in those studies agree with the findings above. Therefore, the findings presented above seem to be independent of the moving ground.

Conclusions

The effects of the rim's geometry on the drag coefficient and flowfield around a vehicle were investigated. A modular wheel concept was developed, which allowed quick modifications to the rim geometry. The effects of 14 different rim geometric parameters on the drag coefficient were investigated using two design of experiment methods, a screening and a detailed parameter investigation. A sedan vehicle and an estate vehicle were used in the investigation to determine the robustness of the results. The same trends were found for the sedan and estate models. It was found that the cooling flow had no impact on the effects of the rim geometric parameters on the vehicle's drag coefficient. Regression models were developed for both vehicles, which allowed the user to obtain the overall drag coefficient given the rim geometric parameter levels. The regression model had a 95% confidence interval of 1.82 counts with respect to the measured values. Flowfield, base pressure, and wheelhouse pressure measurements were also taken. A numerical model (CFD simulation) was developed of the sedan vehicle to further investigate the effects of the total coverage area on the flowfield. This numerical model was validated with the drag and flowfield measurements.

It was found that, the coverage area had the greatest effect on the drag coefficient, where increasing the coverage area decreased the drag coefficient. An equation was found to describe this relationship, and it was found to be inversely proportional, regardless of the cooling flow configuration. The flowfield, pressure measurements, and numerical model showed some reasons for this relationship; increasing the coverage area typically reduced the flow through the rim that otherwise fed the jetting vortex. As a result, the drag caused by the jetting vortex was reduced. An increasing coverage area also increased the base pressure, thereby directly reducing the pressure drag of the vehicle.

The rim cover angle, depth of center, and drop angle were the next most effecting parameters on the drag coefficient, however, their effects were significantly lower than the coverage area. Increasing the rim cover angle increased the drag coefficient, which in the closed cooling configuration was, at least in part, due to a decreased base pressure. Increasing the depth of center or increasing the drop angle also increased the drag coefficient, however, the causes were undetermined.

Little synergy among the rim geometric parameters were found, with only two significant ones occurring; the rim cover distance with the rim cover angle, and the rim cover depth with the rim cover angle. Increasing the rim cover distance along with the rim cover angle increased the drag coefficient, which with closed cooling was at least in part caused by a decreased base pressure. Increasing the rim cover depth and rim cover angle created a step between the spokes and the rim cover, allowing a flow through the wheel, which the jetting vortex and creating more drag; a similar effect as when decreasing the coverage area.

The synergy between the front and rear rims was also investigated, and it was found that the effects of the front and rear rims on the drag were independent of each other. Furthermore, the flow development down the side of the vehicle was largely dominated by the front rim geometry, and the rear rim geometry did not have significant effects on the flow in this region. However, increasing the coverage area at the rear wheel was a more effective way of decreasing the drag coefficient than increasing the coverage area at the front.

References

1. Hucho, W.H., "Aerodynamics of Road Vehicles, Fourth Edition," (Warrendale, SAE International, 1998), ISBN 0768000297.
2. Barnard, R. H., "Road Vehicle Aerodynamic Design, Second Edition," (St Albans: Mechaero Publishing, 2001), ISBN 0954073401.
3. Schütz, T., "Aerodynamics of Road Vehicles, Fifth Edition," (Warrendale, SAE International, 2015), ISBN 0768079772.
4. Council of European Union, "Regulation (EU) No 333/2014 of the European Parliament and of the Council," https://eur-lex.europa.eu/legal-content/EN/TXT/?uri=uriserv%3AOJ.L_.2014.103.01.0015.01.ENG, 2014.

5. Schnepf, B., Schütz, T. and Indinger, T., "Further Investigations on the Flow Around a Rotating, Isolated Wheel and Detailed Tread Pattern," SAE Technical Paper 2015-01-1554, 2015, doi: 10.4271/2015-01-1554.
6. Mayer, W. and Wiedemann, J., "The Influence of Rotating Wheels on Total Road Load," SAE Technical Paper 2007-01-1047, doi: 10.4271/2007-01-1047.
7. Wäschle, A., "The Influence of Rotating Wheels on Vehicle Aerodynamics – Numerical and Experimental Investigations," SAE Technical Paper 2007-01-0107, 2007, doi: 10.4271/2007-01-0107.
8. Qui, Z., "Wheel Aerodynamic Developments by Module-Based Prototype Rims and Stationary Rim Shields," Master's Thesis, Department of Applied Mechanics, Chalmers University of Technology, Gothenburg, 2009.
9. Landström, C., Josefsson, L., Walker, T., and Löfdahl, L., "An Experimental Investigation of Wheel Design Parameters with Respect to Aerodynamic Drag," *9th FKFS Conference*, Progress in Vehicle Aerodynamics and Thermal Management, Stuttgart, 2011.
10. Vdovin, A., Bonitz, S., Landström, C., and Löfdahl, L., "Investigation of Wheel Ventilation-Drag Using a Modular Wheel Design Concept," SAE Technical Paper 2013-01-0953, 2013, doi: 10.4271/2013-01-0953.
11. Kremheller, A., "Development Method for Aerodynamic Wheel Designs using Wind Tunnel and CFD," *EADE Meeting*, UK, 2016.
12. Mercker, E., Breuer, N., Berneburg, H., and Emmelmann, H.J., "On the Aerodynamic Intereference Due to Rolling Wheels of Passenger Cars," SAE Technical Paper 910311, 1999, doi: 10.4271/910311.
13. Croner, E., Bézard, H., Sicot, C., and Mothay, G., "Aerodynamic Characterization of the Wake of an Isolated Rolling Wheel," International Journal of Heat and Fluid Flow, Vol. 43, pp. 233-243, 2013, doi: 10.1016/j.ijheatfluidflow.2013.04.008.
14. Huminic, A. and Huminic, G., "Aerodynamic Study of a Generic Car Model with Wheels and Underbody Diffuser," International Journal of Automotive Technology, Vol. 18, No. 3, pp.397-40, 2017, doi: 10.1007/s12239-017-0040-6.
15. Gleason, M., Duncan, B., Walter, J., Guzman, A., and Cho, Y., "Comparison of Computational Simulation of Automotive Spinning Wheel Flow Field with Full Width Moving Belt Wind Tunnel Results," SAE Technical Paper 2015-01-1556, 2015,
16. Landström, C., Walker, T., Christoffersen, L., and Löfdahl, L., b). "Influences of Different Front and Rear Wheel Designs on Aerodynamic Drag of a Sedan Type Passenger Car," SAE Technical Paper 2011-01-0165, 2011, doi: 10.4271/2011-01-0165.
17. Elofsson, P. and Bannister, M., "Drag Reduction Mechanisms Due to Moving Ground and Wheel Rotation in Passenger Cars," SAE Technical Paper 2002-01-0531, 2001, doi:10.4271/2002-01-0531.
18. Sternéus, J., Walker, T., and Bender, T., "Upgrade of the Volvo Cars Aerodynamic Wind Tunnel," SAE Technical Paper 2007-01-1043, 2007, doi: 10.4271/2007-01-1043.
19. Ljungskog, E., Sebben, S., Broniewicz, A., and Landström, C., "A Parametric Study on the Influence from Boundary Conditions on the Longitudinal Pressure Gradient in CFD Simulations of an Automotive Wind Tunnel," Journal of Mechanical Science and Technology, Vol. 31, pp. 2821-2827, 2017, doi:10.1007/s12206-017-0525-2.
20. Robertsson, V., "Development of a New Cost-Efficient Procedure for Evaluation of Wheel Design Aerodynamic Performance," Master's thesis, Department of Product and Production Development, Chalmers University of Technology, Gothenburg, 2017.
21. Landström, C., "Passenger Car Wheel Aerodynamics," Ph.D. thesis, Department of Applied Mechanics, Chalmers University of Technology, Gothenburg, 2011.
22. Aeropobe, https://www.aeroprobe.com/omniprobe/#1492296220035-2d83d6ab-26fe, August 2018.
23. Landström, C., Löfdahl, L, and Walker, T., "Effects of Ground Simulation on the Aerodynamic Coefficients of Production Car in Yaw Conditions," SAE Technical Paper 2010-01-0755, 2010, doi: 10.4271/2010-01-0755.
24. Siemens, 2017. *STAR-CCM+ User Guide*. Version 12.04.011.
25. Landström, C., Löfdahl, L., Josefsson, L., and Walker, T., "Aerodynamic Effects of Different Tyre Models on a Sedan Type Passenger Car," SAE Technical Paper 2012-01-0169, 2012, doi: 10.4271/2012-01-0169.
26. Hobeika, T. and Sebben, S., "Tyre Pattern Features and Their Effects on Passenger Vehicle Drag," SAE Technical Paper 2018-01-0710, 2019, doi: 10.4271/2018-01-0710.
27. Qiu, Z., Landström, C., Löfdahl, L., and Josefsson, L., "Wheel Aerodynamic Developments on Passenger Cars by Module-Based Prototype Rims and Stationary Rim Shields," *FISTA Automotive World Congress*, Budapest, Hungary, 2010.
28. Bolzon, M.D., Sebben, S., and Broniewicz, A., "The Effects of a Rim's Configuration on a Wheel's Flow Physics," *International Conference on Vehicle Aerodynamics*, Birmingham, UK, 2018.

Contact Information

Adam Brandt – adam.brandt@chalmers.se
Chalmers University of Technology, Sweden

Acknowledgments

The authors would like to thank Michelin© for supplying the models of the deformed tires.

The simulations were performed on resources provided by the Swedish National Infrastructure for Computing (SNIC) at PDC Centre for High Performance Computing (PDC-HPC).

Definitions/Abbreviations

A_{base}	Base Area, m^2
A/C	Air Conditioner
A_i	Area Corresponding to i^{th} Point
BW	Base Wheel (a thin wheel used in the modular wheel concept)
CAC	Charged Air Cooler
CC	Closed Cooling

C_D	Drag Coefficient
$C_{D\ base}$	Base Drag Coefficient
C_{D_L}	Local Drag Coefficient
CFD	Computational Fluid Dynamics
C_P	Static Pressure Coefficient
C_{Pi}	Static Pressure Coefficient for i^{th} point
C_{P_t}	Total Pressure Coefficient
DAQ	Data Acquisition System
DPI	Detailed Parameter Investigation
FFD	Fractional Factorial Design
IDDES	Improved Delayed Detached Eddy Simulation
OC	Open Cooling
P	Pressure, Ps
P_S	Static Pressure, Pa
PW	Production Wheel
P_∞	Freestream Pressure
u	Velocity in the x-direction, m/s
v	Velocity in the y-direction, m/s
V	Velocity, m/s
VCC	Volvo Car Corporation
V_∞	Freestream Velocity, m/s
w	Velocity in the z-direction, m/s
x	Freestream Direction
y	Lateral Direction
z	Vertical Direction
Δ	Change between two quantities
ρ	Density, kg/m^3
ω	Vorticity, 1/s
1 drag count	$\Delta C_D = 0.001$

Appendix A: Screening test matrix and corresponding rim photographs

Table A1. The screening test matrix, using the Plackett-Burman design, with the parameter maximum (+), minimum (-) and center values (0).

Config. \ No.	3	4	5	6	10	8	14	11	9	12
S01	+	-	+	-	-	-	+	+	+	-
S02	+	+	-	+	-	-	-	+	+	+
S03	-	+	+	-	+	-	-	-	+	+
S04	+	-	+	+	-	+	-	-	-	+
S05	+	+	-	+	+	-	+	-	-	-
S06	+	+	+	-	+	+	-	+	-	-
S07	-	+	+	+	-	+	+	-	+	-
S08	-	-	+	+	+	-	+	+	-	+
S09	-	-	-	+	+	+	-	+	+	-
S10	+	-	-	-	+	+	+	-	+	+
S11	-	+	-	-	-	+	+	+	-	+
S12	-	-	-	-	-	-	-	-	-	-
S13	0	0	0	0	0	0	-	0	0	0
S14	0	0	0	0	0	0	+	0	0	0

Figure A1. The screening rim configurations (S01-S14).

Appendix B: Detailed parameter investigation (DPI) test matrix and corresponding rim photographs

Table A2. The detailed parameter investigation matrix, with the parameter maximum (+), minimum (-) and center values (0).

Config. \ No.	1	3	4	2	6	11	7
D01	-	-	-	-	+	-	+
D02	+	-	-	-	-	-	+
D03	-	+	-	-	-	-	+
D04	+	+	-	-	+	-	+
D05	-	-	+	-	-	-	+
D06	+	-	+	-	+	-	+
D07	-	+	+	-	+	-	+
D08	+	+	+	-	-	-	+
D09	-	-	-	+	-	-	+
D10	+	-	-	+	+	-	+
D11	-	+	-	+	+	-	+
D12	+	+	-	+	-	-	+
D13	-	-	+	+	+	-	+
D14	+	-	+	+	-	-	+
D15	-	+	+	+	-	-	+
D16	+	+	+	+	+	-	+
D17	-	-	-	-	-	+	+
D18	+	-	-	-	+	+	+
D19	-	+	-	-	+	+	+
D20	+	+	-	-	-	+	+
D21	-	-	+	-	+	+	+
D22	+	-	+	-	-	+	+
D23	-	+	+	-	-	+	+
D24	+	+	+	-	+	+	+
D25	+	-	-	-	+	-	-
D26	+	+	-	-	-	-	-
D27	+	-	+	-	-	-	-
D28	+	+	+	-	+	-	-
D29	+	-	-	+	-	-	-
D30	+	+	-	+	+	-	-
D31	+	-	+	+	+	-	-
D32	+	+	+	+	-	-	-
D33	0	0	0	0	0	-	+
D34	0	0	0	-	0	0	+
D35	+	0	0	0	0	-	0
D41	+	-	-	+	-	-	+

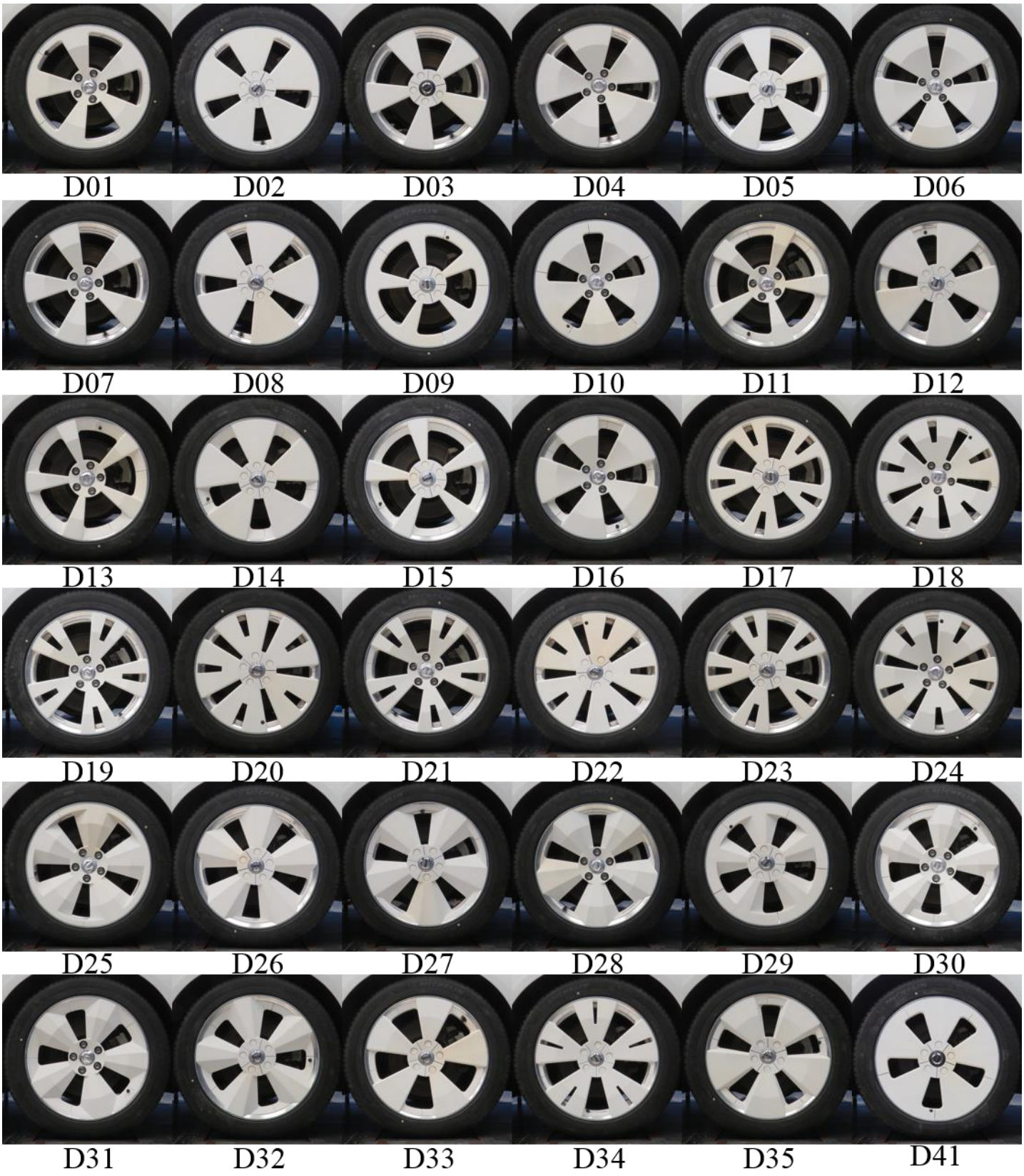

Figure A2: The detailed parameter investigation rim configurations (D01-D35).

Appendix C: The vorticity distribution of the rim geometries investigated in the CFD simulations

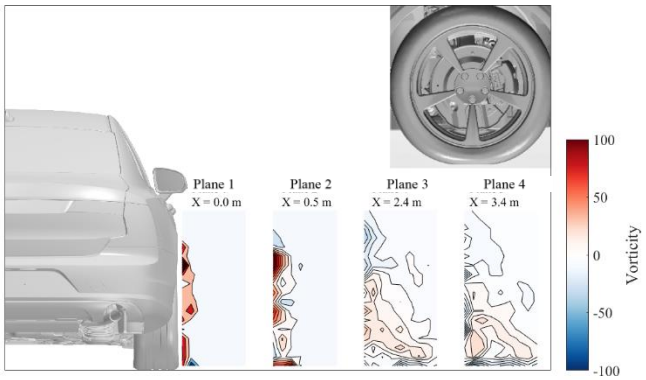

Figure C1. The vorticity distributions of the CFD model with D36 rims. Closed cooling.

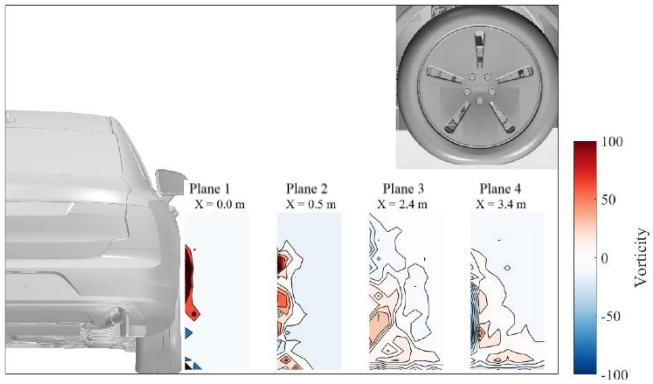

Figure C2. The vorticity distributions of the CFD model with D38 rims. Closed cooling.